JACS
JOURNAL OF THE AMERICAN CHEMICAL SOCIETY

ARTICLE

pubs.acs.org/JACS

Five-Dimensional Incommensurate Structure of the Melilite Electrolyte $[CaNd]_2[Ga]_2[Ga_2O_7]_2$

Fengxia Wei,[†] Tom Baikie,*[,†] Tao An,[†] Martin Schreyer,[‡] Christian Kloc,[†] and Tim J. White[†,§]

[†]Division of Materials Science & Engineering, Nanyang Technological University, 50 Nanyang Avenue, 639798 Singapore

[‡]Institute of Chemical Engineering Sciences (ICES), Agency for Science, Technology and Research, 1 Pesek Road, Jurong Island, 627833 Singapore

[§]Centre for Advanced Microscopy, Australian National University, Sullivan's Creek Road, Canberra, ACT 0200, Australia

Supporting Information

ABSTRACT: Melilite-type gallium oxides are potential intermediate temperature electrolytes for solid oxide fuel cells. Single crystals of $[CaNd]_2[Ga]_2[Ga_2O_7]_2$ grown using an optical floating zone furnace have been investigated using transmission electron microscopy and powder and single-crystal X-ray diffraction. The anion array topologically conforms to a $[(3.5.4.5)^2, 3.5.3.5]$ network that contains distorted pentagonal tunnels. The distortion is necessary to achieve space filling and accommodate structural misfit between the layers. Satisfactory bond lengths and angles are obtained through two-dimensional modulation in the tetragonal based plane, leading to five-dimensional symmetry in the superspace group $P\bar{4}2_1m(\alpha,\alpha,0)00s(\bar{\alpha},\alpha,0)000$, $\alpha = 0.2319(2)$, with modulation vectors $\mathbf{q}_1 = \alpha(\mathbf{a}^* + \mathbf{b}^*)$ and $\mathbf{q}_2 = \alpha(-\mathbf{a}^* + \mathbf{b}^*)$. Both displacive and occupational modulations are found. Through this mechanism, melilites are primed to accommodate mobile oxygen interstitials, suggesting a rational approach to crystallochemical tailoring that will enhance ionic diffusion and optimize electrolyte performance.

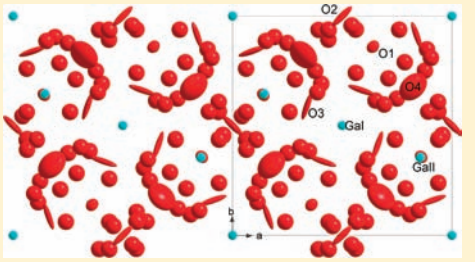

INTRODUCTION

Solid oxide fuel cells (SOFCs) are an efficient and low-polluting energy conversion technology. A focus of current research is to reduce SOFC operating temperatures to ~500 °C through deployment of highly conductive electrolytes. Usually, oxygen transport is mediated via anionic vacancies, typically, in yttria-stabilized zirconia (YSZ) and gadolinium-doped ceria.[1] However, in some materials oxide ions conduct via an interstitial mechanism at "intermediate" temperatures.[2] Of particular interest are the apatite,[3] fergusonite,[4] and melilite[5,6] families, which contain mobile superstoichiometric oxygen. Those structures often show nonrational crystallographic translations, not accommodated within standard three-dimensional crystallographic space groups, but rather superspace groups, which describe periodicity in four, five, and six dimensions.[7] Numerous materials are now classified as higher dimensional structures, including Na_2CO_3,[8] intermetallic quasicrystals,[9] and cuprate high-temperature superconductors,[10] along with certain apatites,[11] fergusonites,[12] and melilites.[13] Of the latter structure types, the melilite family is currently the most broadly understood in terms of incommensurability and ion conduction, but a direct causal link between crystal chemistry and electrolyte performance remains to be established.

To a first approximation, melilites adopt tetragonal $P\bar{4}2_1m$ symmetry and have the general formula $[A_2]_2[B^I]_2[B^{II}{}_2O_7]_2$, where A is a large divalent or trivalent ion (e.g., Ln, Ca, Sr, and Ba) and B^I and B^{II} are symmetrically distinct small cations (e.g., Si and Ge). Two-dimensional extended oxygen networks of the type $[(3.5.4.5)^2, 3.5.3.5]$ are created by corner connection of B^IO_4 and $B^{II}{}_2O_7$ units, with these layers separated by AO_8 polyhedra.[14] This structural framework can accommodate a large excess of oxygen, up to 0.32 per formula unit (e.g., $[Ca_{0.36}La_{1.64}]_2[Ga]_2[Ga_2O_{7.32}]_2$),[15] believed responsible for the high ion conductivity. Misfit of the tetrahedral layers with the interlayer cations is accommodated by atomic displacements, leading to incommensuration, which has been extensively studied in natural and synthetic silicate melilites,[13] but not so deeply for electrolyte compositions. Seifert et al.[16] analyzed åkermanite ($[Ca_2]_2[Mg]_2[Si_2O_7]_2$) using ^{29}Si magic angle spinning nuclear magnetic resonance (MAS NMR) spectroscopy and found an incommensurate to commensurate phase transition at 78 °C. Synthetic $[Ca_2]_2[Co]_2[Si_2O_7]_2$ (Co-åkermanite) was found to be modulated using single-crystal X-ray diffraction,[17] and soon after, the solid solutions of $[(Sr/Ca)]_2[Co/Zn/Mg]_2[Si_2O_7]_2$ were described,[18−21] with specific combinations of A and/or B^I site substitutions resulting in modulation. Bindi et al.[22] reported a natural melilite ($[Ca_{1.89}Sr_{0.01}Na_{0.08}K_{0.02}]_2[Mg_{0.92}Al_{0.08}]_2[Si_{1.97}Al_{0.03}O_7]_2$) was also modulated, while transmission electron microscopy (TEM) defined the incommensurate to commensurate phase transition temperatures of $[(Sr/Ca)]_2[(Co/Mg/Zn/Fe/Cu)]_2[(Si/Ge)_2O_7]_2$ compositions.[13] Almost all previous work has focused on substitutions at the A (4*e*) and B^I (2*a*) cation sites.

Received: July 12, 2011
Published: August 16, 2011

 © 2011 American Chemical Society

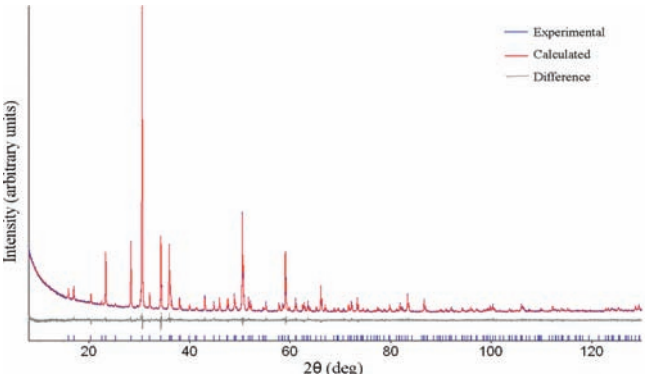

Figure 1. PXRD Rietveld refinement for the $[CaNd]_2[Ga]_2[Ga_2O_7]_2$ subcell (R_B = 1.6%).

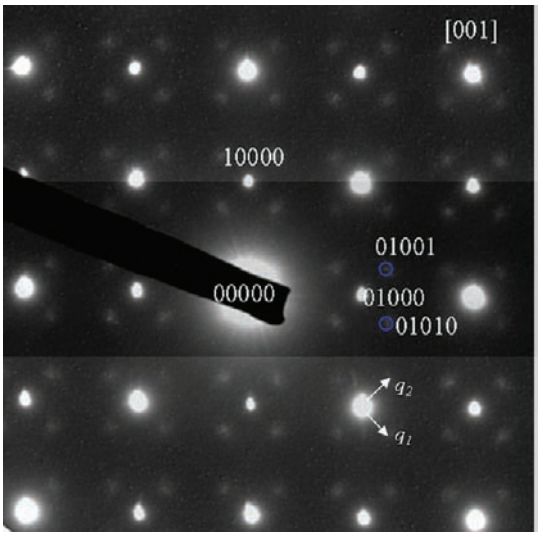

Figure 2. [001] selected area diffraction pattern of $[CaNd]_2[Ga]_2[Ga_2O_7]_2$, showing the $\mathbf{q}_1$ and $\mathbf{q}_2$ modulations.

Table 1. Atomic Coordinates and Isotropic ADPs from PXRD for the $P\bar{4}2_1m$ Average Structure of $[CaNd]_2[Ga]_2[Ga_2O_7]_2$

atom	x	y	z	occupancy	B_{iso}
Ca^1	0.16081(14)	0.66081(14)	0.49232(3)	0.5	0.666(3)
Nd^1	0.16081(14)	0.66081(14)	0.49232(3)	0.5	0.666(3)
Ga^I	0	0	0	1	0.658(3)
Ga^{II}	0.35730(18)	0.85730(18)	0.03628(3)	1	0.658(3)
O^1	0.5	0	0.1928(2)	1	3.05(18)
O^2	0.3555(10)	0.8555(10)	−0.3126(12)	1	3.05(18)
O^3	−0.1634(10)	0.09030(19)	0.2134(11)	1	3.05(18)

As recently shown, the gallate melilite $[Sr_{0.46}La_{1.54}]_2[Ga]_2[Ga_2O_{7.27}]_2$ possesses high oxide conductivity (0.02−0.1 S cm^{-1}) over the temperature range 600−900 °C,[5,15,23,24] and for the $[Ca_{1-x}La_{1+x}]_2[Ga]_2[Ga_2O_{7+x/2}]_2$ series phase transitions from tetragonal ($x \leq 0.5$) to orthorhombic ($0.5 < x \leq 0.6$) to triclinic ($0.6 < x \leq 0.64$) symmetry were found as lanthanum content increased.[15] It was also observed that $x > 0.5$ gave lower conductivities, attributed to the reduction of symmetry; however,

Table 2. Experimental Details

Crystal Data	
chemical formula	$CaNdGa_3O_7$
chemical fw	505.47
temp (K)	293
cell setting	tetragonal
superspace group	$P\bar{4}2_1m(\alpha,\alpha,0)00s(\bar{a},a,0)000$
a (Å)	7.8868(4)
c (Å)	5.2243(3)
vol (Å^3)	324.96(4)
no. of formula units (Z)	2
D_x (Mg m^{-3})	5.139
modulation wave vectors	$\mathbf{q}_1 = 0.2319(2)(\mathbf{a}^* + \mathbf{b}^*)$
	$\mathbf{q}_2 = 0.2319(2)(-\mathbf{a}^* + \mathbf{b}^*)$
cryst form	irregular
cryst size (mm)	0.10 × 0.08 × 0.15
cryst color	purple under sunlight
	blue under fluorescent lamp
Data Collection	
diffractometer	Bruker Smart ApexII four-circle diffractometer
radiation type	Mo Kα
wavelength (Å)	0.71073
abs correction type	multiscan
abs coeff (μ) (mm^{-1})	20.777
range of h, k, l, m, and n	$-12 \rightarrow h \rightarrow +9$
	$-12 \rightarrow k \rightarrow +9$
	$-7 \rightarrow l \rightarrow +5$
	$-1 \rightarrow m \rightarrow +1$
	$-1 \rightarrow n \rightarrow +1$
no. of measured reflns	17097
no. of unique reflns	5249
no. of obsd reflns	2219
no. of main reflns	637
no. of satellites	
for ±(1, 0) ± (0, 1)	1531
for ±(1, 1) ± (−1, 1)	51
criterion for obs reflns	$I > 3\sigma(I)$
Refinement	
refinement on	F
R, R_w (all reflns)	0.0378, 0.0519
R, R_w (main reflns)	0.0236, 0.0316
R, R_w (satellites) for ±(1, 0) ± (0, 1)	0.0645, 0.0721
R, R_w (satellites) for ±(1, 1) ± (−1, 1)	0.1690, 0.1567
S	2.20
no. of params	322
weighting scheme	$w = [\sigma^2(F) + (0.01F)^2]^{-1}$
$(\Delta/su)_{max}$	0.0195
$\Delta\rho_{max}$ (e Å^{-3})	1.41
$\Delta\rho_{min}$ (e Å^{-3})	−1.23
extinction correction	B−C type 1 Lorentzian isotropic (Becker and Coppens, 1974)
extinction coeff	4600(300)
source of atomic scattering factors	International Tables for Crystallography (1992, Vol. C)[31]

dx.doi.org/10.1021/ja206441x | J. Am. Chem. Soc. 2011, 133, 15200–15211

Table 3. Atomic Coordinates and Anisotropic Displacement Parameters for the Average Structure

atom			x	y	z	occu	U_{iso}
Nd^1	4*e*	..*m*	0.15917(5)	0.65917(5)	0.49516(10)	0.489(4)	0.01327(15)
Ca^1	4*e*	..*m*	0.15917(5)	0.65917(5)	0.49516(10)	0.511(4)	0.01327(15)
Ga^I	2*a*	−4..	0	0	0	1	0.0112(2)
Ga^{II}	4*e*	..*m*	0.35651(7)	0.85651(7)	0.03522(14)	1	0.00910(15)
O^1	4*e*	..*m*	0.3599(5)	0.8599(5)	−0.3063(10)	1	0.0210(11)
O^2	2*c*	2.*mm*	0.5	1	0.1990(15)	1	0.033(2)
O^3	8*f*	1	−0.1622(6)	0.0904(12)	0.2082(9)	1	0.049(2)

atom	U_{11}	U_{22}	U_{33}	U_{12}	U_{13}	U_{23}
Nd^1	0.0162(2)	0.0162(2)	0.0073(3)	−0.00759(17)	−0.00014(12)	−0.00014(12)
Ca^1	0.0162(2)	0.0162(2)	0.0073(3)	−0.00759(17)	−0.00014(12)	−0.00014(12)
Ga^I	0.0123(3)	0.0123(3)	0.0089(5)	0	0	0
Ga^{II}	0.0106(2)	0.0106(2)	0.0061(3)	0.0013(2)	0.00164(15)	0.00164(15)
O^1	0.0262(18)	0.0262(18)	0.011(2)	−0.013(3)	0.0028(13)	0.0028(13)
O^2	0.048(4)	0.048(4)	0.002(3)	−0.032(5)	0	0
O^3	0.022(2)	0.109(6)	0.0167(19)	0.034(3)	−0.0128(18)	−0.025(3)

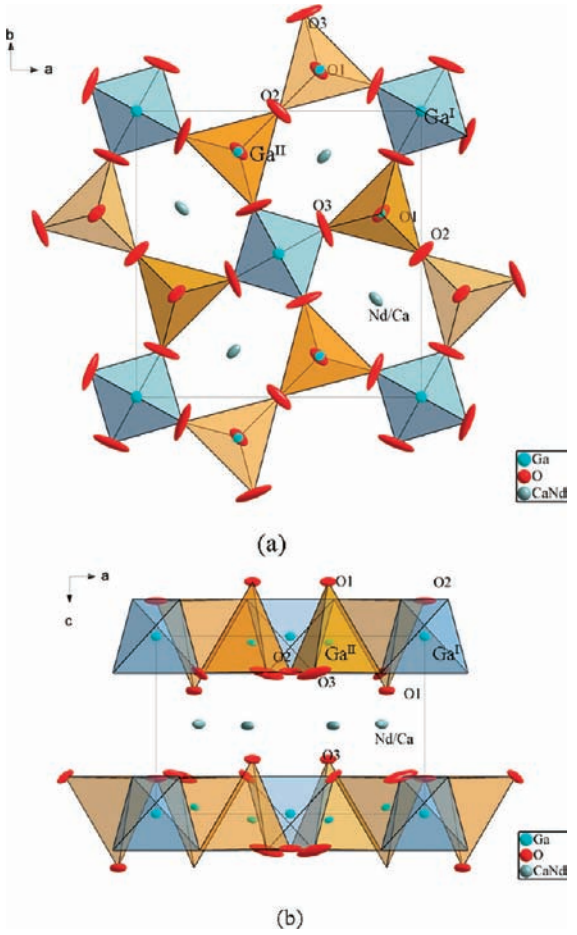

Figure 3. Average structure of $[Ca_2Nd_2][Ga]_2[Ga_2O_7]_2$, obtained through single-crystal X-ray diffraction. Projected along (a) ⟨001⟩ and (b) ⟨010⟩. Atoms are represented by 50% probability displacement ellipsoids.

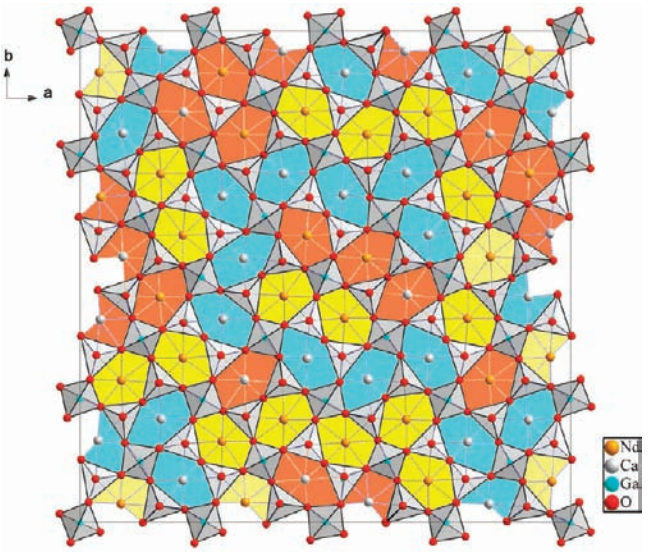

Figure 4. Approximate modulated structure of the $4a \times 4a \times 1c$ cell, projected along the *c* axis. Nd/Ca−O bonds of <2.9 Å are represented by sticks. Six-coordinate Nd/Ca pentagons are highlighted in aqua, seven-coordinate pentagons are orange, and eight-coordinated pentagons are yellow. The Ga^IO_4 and $Ga^{II}O_4$ tetrahedra are shown in gray.

Figure 5. Eight-, seven-, and six-fold coordination of the A site cations. Bonds longer than 2.9 Å are represented by dashed lines. The atomic coordinates were at $t = 0$, $u = 0$; $t = 0.5$, $u = 0.5$; and $t = 0.6$, $u = 0$, respectively. For the symmetry codes refer to Table 4.

no information concerning the nature of the incommensurate modulation in these gallium melilites was provided. Here, we report for the first time the 5D incommensurate structure of the gallium oxide melilite $[CaNd]_2[Ga]_2[Ga_2O_7]_2$ using superspace

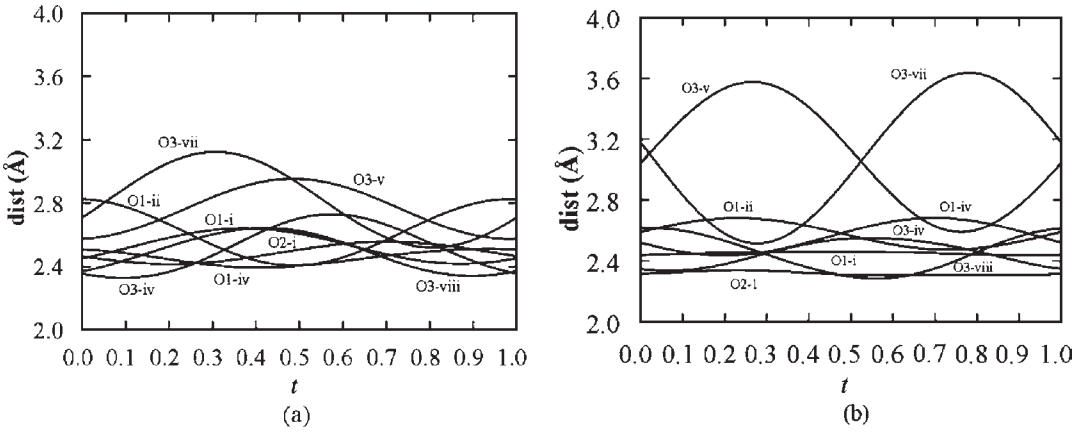

Figure 6. Variation of A−O bond distances as a function of t at (a) $u = 0$ and (b) $u = 0.610$. At some regions, A−O^3 bonds exceed 2.9 Å. Symmetry codes are given in Table 4.

Table 4. Modulated Structure: Interatomic Distances (Å) and Tetrahedral Angles (deg)[a]

	average	minimum	maximum
	A−O Polyhedra		
O^1-i	2.45(7)	2.37(8)	2.53(8)
O^1-ii	2.58(8)	2.38(8)	2.82(8)
O^1-iv	2.57(8)	2.38(8)	2.83(8)
O^2-i	2.42(5)	2.28(5)	2.56(5)
O^3-iv	2.48(6)	2.24(6)	2.74(6)
O^3-v	2.90(6)	2.42(6)	3.64(6)
O^3-vii	2.90(6)	2.42(6)	3.65(6)
O^3-viii	2.49(6)	2.24(6)	2.76(6)
	Ga^IO_4 Tetrahedra		
Ga^I-O^3	1.83(6)	1.68(6)	1.98(6)
O^3-i−Ga^I−O^3-ii	110(3)	90 (2)	131(3)
O^3-i−Ga^I−O^3-iv	107(3)	102(3)	113(3)
O^3-i−Ga^I−O^3-v	110(3)	90(2)	131(3)
O^3-ii−Ga^I−O^3-iv	110(3)	90(2)	131(3)
O^3-ii−Ga^I−O^3-v	107(3)	102(3)	113(3)
O^3-iv−Ga^I−O^3-v	110(3)	90(2)	131(3)
	$Ga^{II}O_4$ Tetrahedra		
$Ga^{II}-O^1$	1.79(8)	1.72(9)	1.87(9)
$Ga^{II}-O^2$	1.82(6)	1.77(7)	1.86(5)
$Ga^{II}-O^3$	1.84(6)	1.69(6)	2.05(6)
O^1-i−Ga^{II}−O^2-i	117(3)	114(3)	120(3)
O^1-i−Ga^{II}−O^3-iv	119(3)	111(3)	131(3)
O^1-i−Ga^{II}−O^3-viii	119(3)	111(3)	130(3)
O^2-i−Ga^{II}−O^3-iv	100(4)	87(4)	112(4)
O^2-i−Ga^{II}−O^3-viii	100(4)	87(4)	112(4)
O^3-iv−Ga^{II}−O^3-viii	97(3)	82(3)	110(2)

[a] Symmetry codes: (i) x, y, z; (ii) $y, -x, 1-z$; (iii) $x, y, -1+z$; (iv) $-x, -y, -1+z$; (v) $-y, x, 1-z$; (vi) $x, y, 1+z$; (vii) $1/2+x, 1/2-y, 1-z$; (viii) $1/2-y, 1/2-x, z$. x, y, and z are the average atomic coordinates in space group $P\bar{4}2_1m$.

formalism[25] and consider the implications with respect to preferential oxygen ion migration pathways, tailoring interstitial oxygen content and enhancing ion mobility.

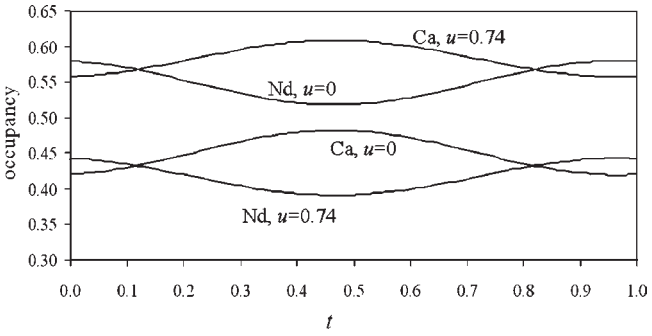

Figure 7. Occupancy variation for the A site atoms Nd and Ca at different u values as a function of t.

EXPERIMENTAL DETAILS

Powder Synthesis. Single crystals of $[CaNd]_2[Ga]_2[Ga_2O_7]_2$ were grown using an optical floating zone furnace. In 10 g batches, stoichiometric mixtures of Nd_2O_3 (99.99%, Alfa Aesar), $CaCO_3$ (99.9%, Alfa Aesar), and Ga_2O_3 (99.999%, Aldrich) were ground and homogeneously mixed in ethanol, dried in air (100 °C, 6 h), and then fired (800 °C, 10 h) to decompose $CaCO_3$. The Nd_2O_3 was dehydrated and decarbonated (1000 °C, 6 h) before use. The calcines were reground, pressed into pellets, and sintered (1400 °C, 12 h) to yield single-phase products according to powder X-ray diffraction (see below). For these experiments, a neodymium melilite rather than the lanthanum analogue was prepared, as the blue color of the former better absorbs infrared radiation, which simplifies single-crystal growth.

Single-Crystal Growth. The polycrystalline materials were isostatically pressed into duplicate cylinders (5 cm × 0.5 cm) to serve as the feed and seed rods and sintered (1400 °C, 6 h) before being mounted in the mirror furnace. Crystal growth took place in an FZ-T-4000-H-VPO-VII-PC optical floating zone furnace (Crystal Systems Corp., Japan) containing four 1.5 kW halogen lamps, with corresponding ellipsoidal mirrors to focus the infrared irradiation to a region ~5 mm in extent, while a constant flow of dry air (2 L/min) passed through the growth chamber. With the onset of melting, tips of the feed and seed rods were brought into contact to form the floating zone, and upon stabilization, the entire mirror stage was raised at a rate of 5 mm/h for crystal growth. The rods were counter-rotated at constant speed (27 rpm) to maintain a stable and well-mixed molten zone. Initially, polycrystalline rods were used as seeds; however, once an appreciable single crystal was obtained, it was cut and oriented with c parallel to the growth direction for subsequent experiments.

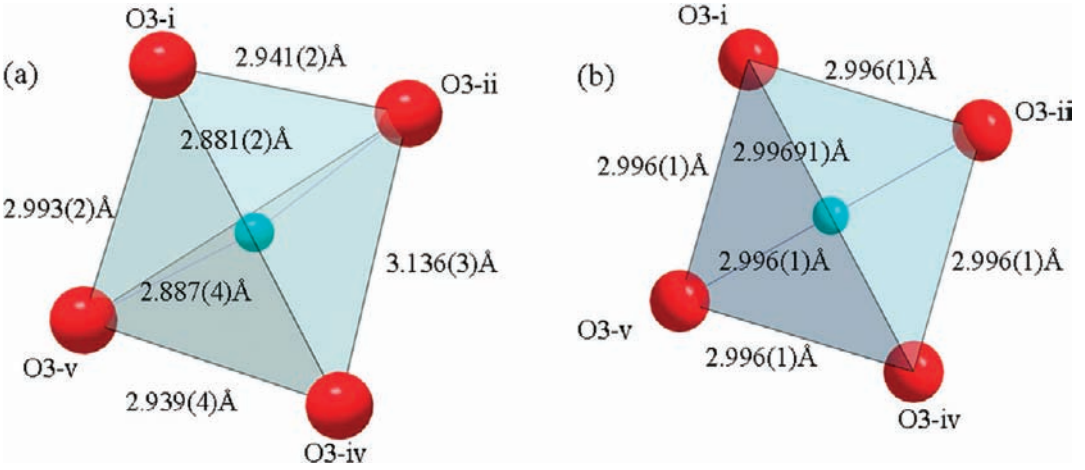

Figure 8. (a) Distorted and (b) undistorted $Ga^{I}O^{3}_{4}$ tetrahedra, viewed along the *c* axis. (a) is extracted from the approximate $4a \times 4a \times 1c$ cell of the modulated structure. Symmetry codes are shown in Table 4.

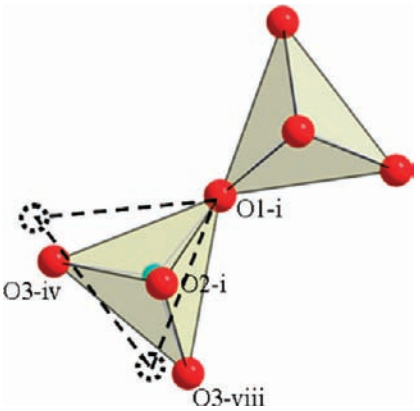

Figure 9. Bent $Ga^{II}_{2}O_{7}$ tetrahedral dimers. Dashed lines show the ideal position, viewed along the *c* axis. Symmetry codes are listed in Table 4.

Structural Characterization. *Powder X-ray Diffraction.* The top and bottom parts of the single-crystal rods were cut and ground for analysis by powder X-ray diffraction (PXRD) to confirm melilite synthesis and check for secondary phases. The PXRD patterns were collected on a Bruker Advance D8 X-ray diffractometer (Cu Kα, λ_{av} = 1.54187 Å) equipped with a Cu Kα X-ray tube operated at 40 kV and 40 mA. The crushed powders were mounted in a top-loaded trough and data accumulated from $2\theta = 5°$ to $2\theta = 140°$ using a step size of 0.02° with a dwell time of 1 s per step. Under these conditions the intensity of the strongest peak was ~30000 counts (Figure 1). Rietveld refinement of the patterns was carried out with TOPAS, version 4.1,[26] using the fundamental parameters approach[27] and a full axial divergence model.[28] The data were refined from the average three-dimensional structure ($P\bar{4}2_1m$), based on the atomic positions of Skakle et al.,[29] in addition to the zero error, Chebyshev polynomial fitting of the background, and "crystallite size" to account for microstructure-controlled line broadening. Only isotropic atomic displacement parameters (ADPs) were refined with a common ADP taken for all O positions and Nd and Ca occupying the same crystallographic site.

Single-Crystal X-ray Diffraction. A single-crystal fragment (0.1 mm × 0.08 mm × 0.15 mm) was cleaved and mounted on a glass fiber. Data were collected on a Bruker Smart Apex II single-crystal diffractometer (X-ray radiation Mo Kα, λ = 0.71073 Å) over an angular range of $2.07° \leq \theta \leq 33.68°$, with an exposure time of 200 s/deg to give a total collection time of ~50 h. The modulation vectors were calculated by the least-squares method from 1891 satellites and reflections indexed with Apex II software using five integer values. The Saint module, deployed within Apex II, was used for reflection integration, performing Lorentz polarization and multiscan absorption corrections. The data were refined using Jana2006,[30] and no extra absorption correction was applied.

Selected Area Electron Diffraction. Selected area electron diffraction (SAED) patterns of single crystals were obtained from powders finely crushed under ethanol with several drops of the suspension deposited on a holey carbon mesh supported by a copper grid. A JEOL field emission TEM 2100F operated at 200 kV and fitted with a CCD camera was used to record the diffraction patterns. A Gatan double tilt holder was employed to tilt crystals to the principal crystallographic orientations, and observations were made with a defocused electron beam. The satellite reflections were extremely weak, and long exposure times (up to 80 s) were required to record these features; only first-order satellites were observed. In general, preferred cleavage favored the location of the [100] zone axis rather [001], although the latter was most informative for direct observation of modulation vectors (Figure 2). Using this procedure, long observation times were possible using a parallel, defocused beam. However, high-resolution microscopy was not feasible as more converged electron probes lead to rapid amorphization.

RESULTS

Crystal Growth. Single crystals up to 5 mm in the long dimension were obtained; it was not possible to grow larger crystals due to crack propagation initiated by crystallographic stresses arising from misfit of the tetrahedral network and the interlayer cations. In this respect, it is noted that single crystals with larger interlayer species (e.g., Sr rather than Ca) were easily obtained even with a very high growth speed (10 mm/h); the structural details of the commensurate Sr-melilites that conform to $P\bar{4}2_1m$ will be reported elsewhere.

Powder X-ray Diffraction. Rietveld refinement of the average structure confirmed single-phase melilite, with no evidence of secondary products (Figure 1). The resultant isotropic ADPs are 0.67(3) Å for Nd/Ca, 0.66(3) Å for Ga, and 3.05(18) Å for oxygen (Table 1), with the latter a probable indication of modulation, but as no satellite reflections were observed, detailed examination was not attempted.

Single-Crystal X-ray Diffraction. As a two-dimensionally modulated structure, all reflections for $[CaNd]_2[Ga]_2[Ga_2O_7]_2$ were indexed using five integers (h, k, l, m, n): $\mathbf{H} = h\mathbf{a}^* + k\mathbf{b}^* + l\mathbf{c}^* + m\mathbf{q}_1 + n\mathbf{q}_2$, where $\mathbf{a}^*$, $\mathbf{b}^*$, and $\mathbf{c}^*$ are the reciprocal lattice vectors.

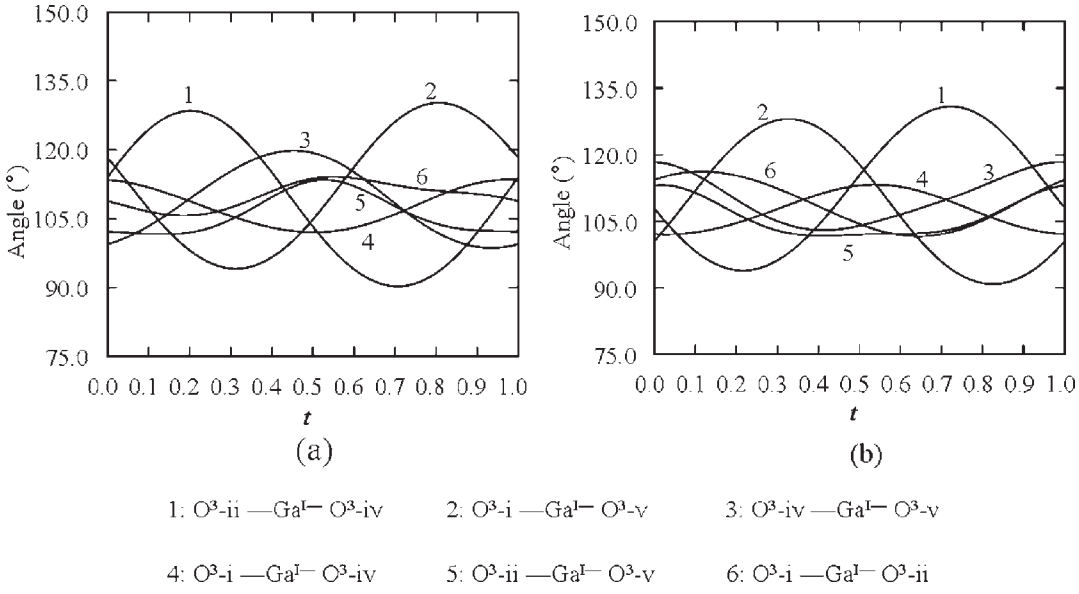

Figure 10. Bond angle variations for $Ga^{I}O^{3}_{4}$ tetrahedra as a function of t at (a) $u = 0$ and (b) $u = 0.5$. Symmetry codes are given in Table 4.

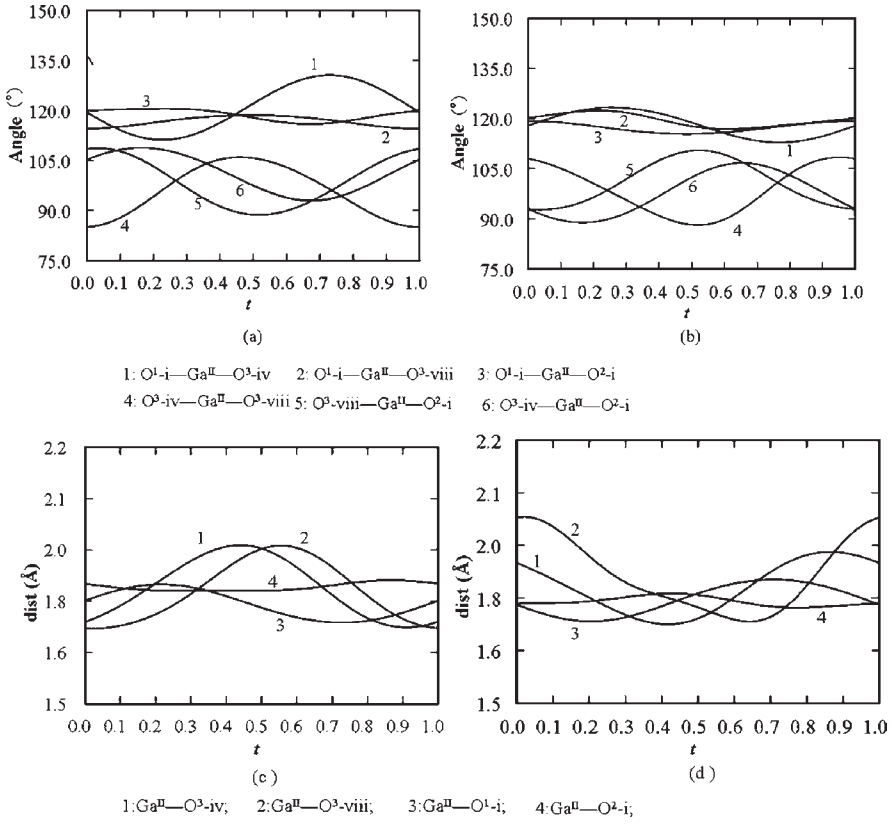

Figure 11. Bond angle (a, b) and bond length (c, d) variations for the $Ga^{II}O_4$ tetrahedron as a function of t at (a, c) $u = 0$ and (b, d) $u = 0.50$. The symmetry codes are the same as in Table 4.

The modulation vectors $\mathbf{q}_1 = 0.2319(2)(\mathbf{a}^* + \mathbf{b}^*)$ and $\mathbf{q}_2 = 0.2319(2)(-\mathbf{a}^* + \mathbf{b}^*)$ were determined by 637 main reflections and 1891 satellite reflections. Experimental and refinement details are collected in Table 2.

Selected Area Diffraction Pattern. The [001] pattern was composed of the main reflections and first-order satellites that can be indexed by five integers, $\mathbf{H} = h\mathbf{a}^* + k\mathbf{b}^* + l\mathbf{c}^* + m\mathbf{q}_1 + n\mathbf{q}_2$ (Figure 2). The first-order satellites form a square around the principal reflections, consistent with tetragonal symmetry. The modulation vectors $\mathbf{q}_1{}^s = 0.234(\mathbf{a}^* + \mathbf{b}^*)$ and $\mathbf{q}_2{}^s = 0.234(-\mathbf{a}^* + \mathbf{b}^*)$ are in good agreement with those obtained by single-crystal X-ray diffraction.

Superspace Group Description. The five-dimensional incommensurate structure can be visualized as a three-dimensional physical object combined with two higher dimensions.

The corresponding superspace group contains the symmetry of the basic structure, plus the symmetry elements in the higher dimension, and for melilite, the superspace group symbol $P^{P\bar{4}2_1m}_{p^4mg}$ (notation according to Janner et al.[32]) was adopted; a comprehensive explanation of this terminology is given by Bindi et al.[33] The upper terms refer to the basic structure, with the lower part representing the respective higher dimensional symmetry operations. For example the $\bar{4}$ superscript directly above the 4 subscript means there is 4-fold inversion in physical space and 4-fold rotation in the higher dimension, 2_1 over m indicates a mirror plane in addition to the screw axis in the 3D space, and the last pair shows a glide related to the mirror symmetry m.

Stokes et al.[34] have recently derived all the (3 + 2) superspace groups and suggested an extended formalization. Accordingly, $[CaNd]_2[Ga]_2[Ga_2O_7]_2$ adopts the melilite basic metric a = 7.8868(4) Å and c = 5.2243(3) Å with two incommensurate modulation vectors, $\mathbf{q}_1 = 0.2319(2)(\mathbf{a}^* + \mathbf{b}^*)$ and $\mathbf{q}_2 = 0.2319(2)(-\mathbf{a}^* + \mathbf{b}^*)$, resulting in a superspace group $P\bar{4}2_1m(\alpha,\alpha,0)00s(\bar{a},a,0)000$, where $\alpha = 0.2319(2)$ is the magnitude of the modulation vectors and $s = 1/2$ indicates an intrinsic translation, which corresponds to the glide plane in the notation of Janner.[32]

Table 5. Bond Valence Sums

			modulated structure		
	formal value	average structure	mean value	minimum	maximum
Nd/Ca	2.5	2.02(10)	2.09(12)	1.79(3)	2.44(3)
Ga^{I}	3	3.14(2)	3.09(3)	2.94(10)	3.56(10)
Ga^{II}	3	3.21(2)	3.15(11)	2.62(10)	3.69(3)

Refinement of Single Crystal XRD Data. The average structure in physical space was refined using the 637 main reflections with $I > 3\sigma(I)$ and quickly converged to $R^{all}_{obsd} = 0.0297$, with the composition $[Ca_{1.023(3)}Na_{0.977(3)}]_2[Ga]_2[Ga_2O_7]_2$, which is close to the notional $[CaNd]_2[Ga]_2[Ga_2O_7]_2$. Table 3 lists the refined atomic coordinates and anisotropic displacement parameters for the average structure. To refine the 5D structure, modulations of both atomic position and displacement parameters were applied using the satellite reflections (1, 0), (0, 1), (1, 1), and (−1, 1). The number of observed (1, 1) and (1, −1) satellites was found to be very low due to the fact that $\alpha \approx 1/4$, and the second-order satellites (h, k, l, 1, 1), (h + 1, k, l, −1, 1), (h, k, l, 1, −1), and (h, k + 1, l, −1, −1) cannot be separated, leading to a relatively high R^{2nd}_{obsd} factor (∼0.17) for second-order satellites. Overlap correction was applied during the refinement by treating pairs of combined satellites as fully overlapped reflections. Separate refinements of first- and second-order satellites were performed, and inclusion of the small number of observed second-order satellites, together with first-order satellites, lowered the R_{obsd} factors, especially R^{1st}_{obsd} by about 12% (from 0.072 to 0.064). Nd/Ca also exhibits occupational modulations, leading to a significant R^{all}_{obsd} reduction (from 0.049 to 0.036).

DISCUSSION

Average Structure. In the average structure, the GaO_4 tetrahedra form pentagonal rings that stack along [001] to create channels. The Nd/Ca cations align as chains inside these channels and

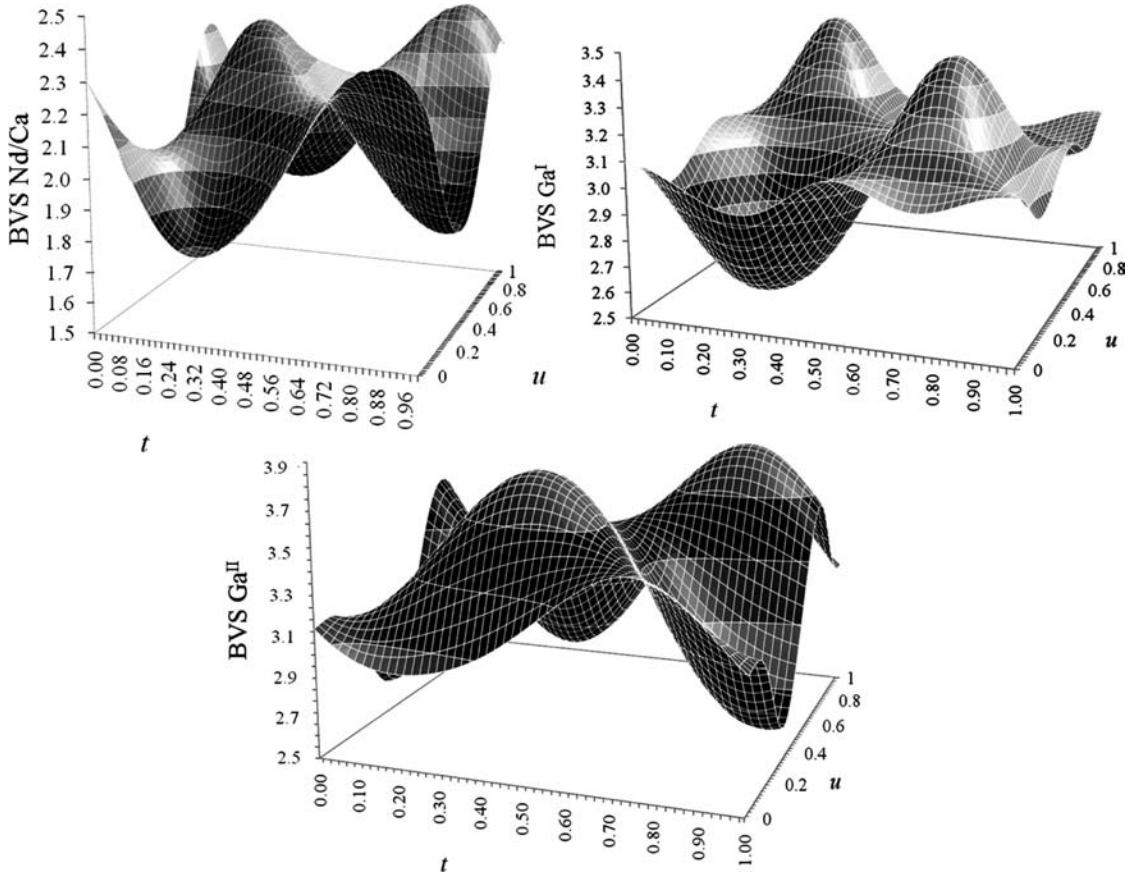

Figure 12. BVS variations for A and B site atoms as a function of t and u. BVS was calculated according to the ratio of Nd to Ca at different t and u values.

are positioned between the layers (Figure 3). The average structure features a strong anisotropy of the Nd/Ca and O displacement ellipsoids; O^2 has the longest ellipsoidal axis directed along ⟨110⟩. $Ga^{II}-O^2-Ga^{II}$ is linear, but O^2 has a large atomic displacement parameter perpendicular to the $Ga^{II}-O^2$ vector; this suggests bending of the $Ga^{II}-O^2-Ga^{II}$ bond, and the real $Ga^{II}-O^2$ distance is longer. This observation is consistent with twisting of the $Ga^{II}{}_2O_7$ tetrahedral dimers around ⟨001⟩, accommodated by a slight rotation of the Ga^IO_4 tetrahedra, probably also along ⟨001⟩. O^3 elongates toward the A site atoms, due to the size misfit of the interstices and the Nd/Ca ionic size.

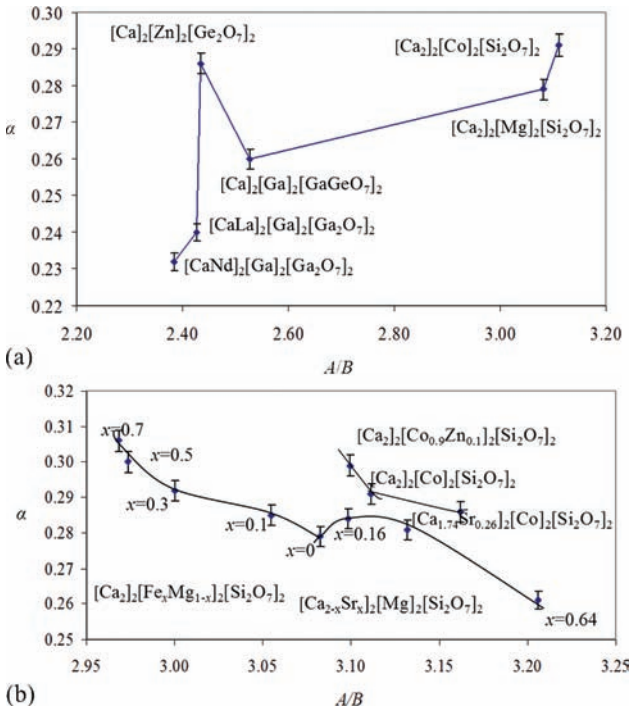

Figure 13. Relationship of α with cation ratio A/B: (a) for end member compositions, (b) for cation substitutions at A or B sites. Ionic radii are calculated according to their respective ratio. α for $[Ca_2]_2[Fe_xMg_{1-x}]_2[Si_2O_7]_2$ is recalculated from Seifert et al.,[37] with $[Ca_2]_2[Co_{0.9}Zn_{0.1}]_2[Si_2O_7]_2$ from Jia et al.,[38] $[Ca_{2-x}Sr_x]_2[Co]_2[Si_2O_7]_2$ from Bagautdinov et al.,[21] and $[Ca_{2-x}Sr_x]_2[Mg]_2[Si_2O_7]_2$ from Jiang et al.[20] $[CaLa]_2[Ga]_2[Ga_2O_7]_2$ and $[Ca_2]_2[Ga]_2[GaGeO_7]_2$ are obtained from SAED (see Figure 14).

Modulated Structure. An approximant $4a \times 4a \times 1c$ cell illustrates the modulation (Figure 4). Deformation of the pentagonal rings is clear and gives rise to a change of coordination around the A cations. Six-, seven-, and eight-coordinate A cations exist in different parts of the structure, assuming A−O distances >2.9 Å are disregarded. The A−O bonds, especially the longest ones, are strongly influenced by the displacive modulation, whereby lengthening and shortening are imposed in different regions of the crystal, leading to a change in the A site coordination (Figure 5). For example, the largest modulations are observed at the longest bonds $A-O^3$-v,vii, with a deviation of bond lengths up to 1.18(2) Å, while the second longest bonds A−O3-iv,viii have differences below 0.52(2) Å. Smaller influences are exerted on the shorter $A-O^1$-i bond; the regular Nd/Ca$-O^1$-i bond is 2.383(2) Å,[35] while the stretched average distances are 2.45(8) Å, varying from 2.37(8) to 2.53(8) Å in the modulated structure. Variations of bond distances caused by modulation can be observed as a function of t and u, the additional two-dimensional space coordinates. For instance, in Figure 6, at some regions, the $A-O^3$ bonds show the greatest variance in excess of 2.9 Å, while the strong short bonds $A-O^2$, and $A-O^1$ are more constant (Table 4). The A−O bond distributions at $t = 0$, $u = 0$ show that there are 35.9% eight-, 29.6% seven-, and 34.5% six-coordinate A−O polyhedra. Occupational modulation is also found for the A site Nd/Ca atoms; at $u = 0$, the occupancy of Nd varies from 0.518(12) to 0.580(12) while that of Ca ranges from 0.420(13) to 0.472(13) as a function of t (Figure 7). Nd-rich and Ca-rich areas can be found at different regions of t and u. Areas of strongest polyhedral distortion correspond to a Ca-rich area, where almost all the six-coordinated polyhedra emerge (Figure 4).

Because the interlayer A cations are too small, compared with the space between the layers, the tetrahedral sheets must distort. The strongest distortion occurs for the $Ga^IO^3{}_4$ tetrahedron (Figure 8), which is compromised by bending of the $Ga^{II}{}_2O_7$ tetrahedral dimers (Figure 9) to stabilize the structure. Positional disorder is introduced into the structure because of this distortion, and consequently, modulation develops. Smaller A cations give rise to larger distortions, and therefore, the structure is more likely to be incommensurate. For a regular $Ga^IO^3{}_4$ tetrahedron in the average structure, the Ga−O bond is 1.8242(4) Å; however,

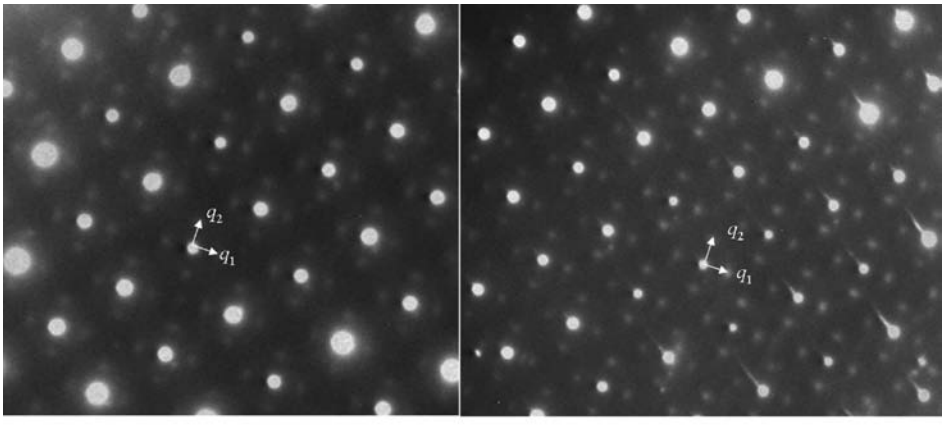

Figure 14. SAED for $[CaLa]_2[Ga]_2[Ga_2O_7]_2$ and $[Ca_2]_2[Ga]_2[GaGeO_7]_2$, showing modulation vectors of ~0.24 and ~0.26, respectively.

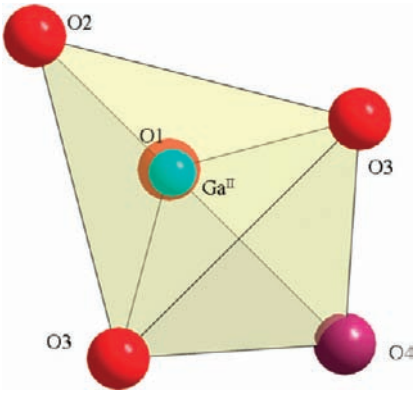

Figure 15. Distorted trigonal bipyramidal $Ga^{II}O_5$. O^4 represents the interstitial oxygen, viewed along the *c* direction.

the modulation distributes the $Ga^{I}O^{3}_{4}$ bond lengths from 1.68(6) to 1.98(6) Å (Table 4). The $O^3-Ga^I-O^3$ bond angle variations are shown in Figure 10, with the largest deviation around 21.50(11)° from the regular tetrahedral angle of 109.49°. In the $Ga^{II}O_4$ tetrahedron, the largest distortion occurs for the O^3-iv—Ga^{II}—O^3-viii angle as well as the $Ga^{II}-O^3$ bonds, with variation of ±17.25(4)° from the average structure (99.246°), and bond length variation of 0.36(12) Å can be found throughout the structure (Figure 11).

Bond Valence Summations. The bond valence sums (BVSs) for all the cations were calculated to evaluate the validity of the structure (Table 5.) The BVSs of Nd/Ca were obtained by summing the partial bond valence of Nd and Ca through the occupancy ratios along *t* and *u* using the parameters of Altermatt and Brown[36] (Figure 12). Similar to the reported incommensurate structure $[Ca_2]_2[Co]_2[Si_2O_7]_2$,[21] the values for Nd/Ca are remarkably lower than the formal charges, consistent with the interstices being too large for the A site cations. High BVS regions correspond to the areas with Nd occupancy dominant, probably because of the larger affinity of Nd^{3+} ions to oxygen. The BVS values for Ga^I and Ga^{II} show large variations, but their mean values are within a tolerable range. In fact, aside from the remarkable variation, the mean values of BVS for all cations in the modulated structure are closer to the formal values than those calculated for the average structure (Table 5).

Modulation Vectors. While the number of fully determined modulated melilite structures remains quite small, sufficient data are now available to search for crystallochemical correlations. The value of α for $\mathbf{q}_1$ and $\mathbf{q}_2$ can be related to the chemical composition, particularly the A/B ionic radius ratio (Figure 13). Cation substitutions at the different sites are found to have distinct effects on the modulation vector. For example, substitutions of larger ions at the B site leads to an increase in α, while similar substitutions at the A site generally induce the opposite effect; e.g., in $[Ca_2]_2[Fe_xMg_{1-x}]_2[Si_2O_7]_2$,[37] increasing the Fe content ($r(Fe^{2+}) > r(Mg^{2+})$) causes α to increase, while α decreases when the Sr content increases in $[Ca_{1-x}Sr_x]_2[Mg]_2[Si_2O_7]_2$[38] and $[Ca_{1-x}Sr_x]_2[Co]_2[Si_2O_7]_2$[21] ($r(Sr^{2+}) > r(Ca^{2+})$). Both situations accommodate increasing α when the A/B ratio decreases, which results in less structural distortion. However, some melilite compositional joins do not always obey the same trend, indicating that, along with the A/B size ratio, different charge combinations for species occupying the same crystallographic site are also important. For example, it is seen that α increases

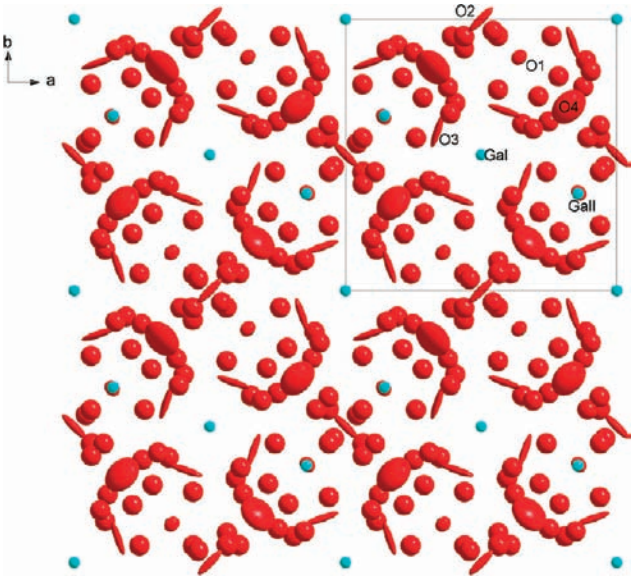

Figure 16. Interstitial oxygen preferred migration path along O^2 and O^3, with no excess electron density indicating migration involving O^1. Fourier peaks are included in the form of oxygen in this representation and are shown in red. The structural representation was derived from a single-crystal X-ray diffraction refinement of $[Ca_{0.5}Nd_{1.5}]_2[Ga]_2[Ga_2O_{7.25}]_2$.

along with the A/B ratio when 4% of Ca is replaced by Sr in $[Ca_2]_2[Mg]_2[Si_2O_7]_2$,[20] and this may reflect ordering of the A cations. Similarly, for $[CaNd]_2[Ga]_2[Ga_2O_7]_2$ and $[CaLa]_2[Ga]_2[Ga_2O_7]_2$, enhanced ordering is expected for the latter because the larger cation size difference will give a larger α. In another example, the tetrahedral size deviation of ZnO_4 and GeO_4 is probably responsible for the abrupt α discontinuity of $[Ca]_2[Zn]_2[Ge_2O_7]_2$. In this review of melilite modulation, the only case that cannot be explained by these systematics is for $[Ca_2]_2[Mg]_2[Si_2O_7]_2-[Ca_2]_2[Co]_2[Si_2O_7]_2$, where the Co^{2+} (0.56 Å) ionic radius is slightly smaller than that of Mg^{2+}(0.57 Å),[35] but α is significantly larger. Possibly, crystal field effects for Co^{2+} account for this apparent anomaly. Moreover, at room temperature, $[Ca_2]_2[Mg]_2[Si_2O_7]_2$ is close to its incommensurate—commensurate phase transition temperature (~80 °C), and the abrupt decrease in α may precede the onset of this transformation.[39] It is notable that for the related $[A_2]_2[B]_2[M_2O_8]_2$ fresnoite materials similar trends have not yet been established. It is suggested this may be due to the prevalence of nanoscale intergrowths of commensurate and incommensurate domains which mask simple correlations between α and compositions.[40]

The existence of eight-, seven-, and six-coordinated A site polyhedra is a distinct feature of the $[CaNd]_2[Ga]_2[Ga_2O_7]_2$ incommensurate structure. Strong distortions of the Ga—O tetrahedra are induced by the variation of interatomic distances. As the incommensurate modulation is due to the misfit between the tetrahedral layers and the size of interlayer cations, smaller A site cations with respect to the B site tetrahedra give rise to greater structural misfit, resulting in incommensurate structures and the internal strain that makes the growth of appreciable single crystals more difficult. Therefore, modulation is predicted when Nd/Ca is substituted with smaller lanthanides such as Sm and Gd or if a larger metalloid enters the B site (e.g., Mg).

Preferred Diffusion Pathways. The preferred crystallochemical formula is $[Ca_{1-x}Nd_{1+x}]_2[Ga]_2[Ga_2O_{7+x/2}]_2$ as this provides

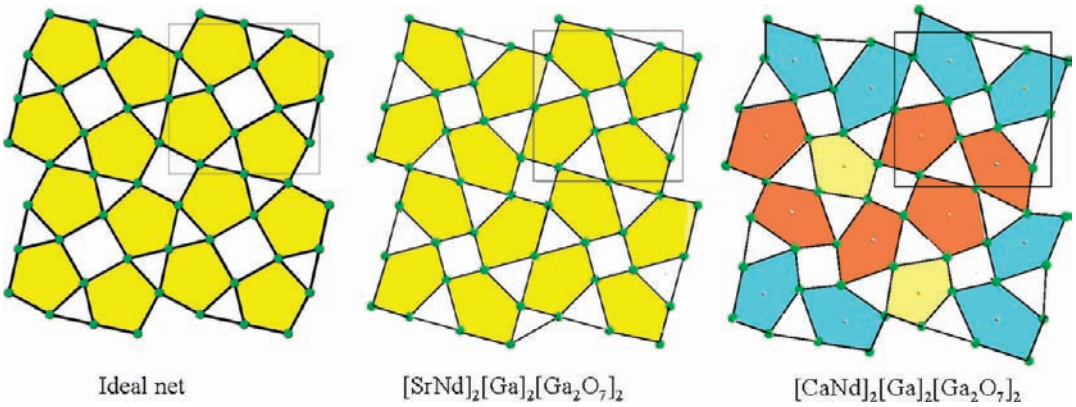

Figure 17. Projected topologies of the $[(3.5.4.5)^2, 3.5.3.5]$ tetrahedron−pentagon oxygen nets of melilite. The ideal net is from O'Keeffe and Hyde.[14] $[SrNd]_2[Ga]_2[Ga_2O_7]_2$ is a commensurate derivative, and $[CaNd]_2[Ga]_2[Ga_2O_7]_2$ is modulated. Obvious pentagon distortion can be observed in both nonmodulated and modulated nets. Six-, seven-, and eight-coordinated polyhedra are filled by aqua, orange, and yellow colors, respectively.

Table 6. Planar Pentagonal Nets with the Highest Proportion of Pentagons May Be Especially Suitable for Ion Conduction

net[14]	vertices	pentagon/quadrangle/triangle ratio (%)	examples
20	$[(3.5.4.5)^2, 3.5.3.5]$	40/20/40	melilite, fresnoite, $Ca_5Al_6O_{18}$[41]
21	$[5.4^3, 5.4.3.4, 5.4^3, (5.4.3.4)^2]$	20/60/20	$K_3W_5O_{15}$[14],
22	$[(5^3.3)^2, 5^3, 5^3.3, 5^3]$	66.7/0/33.3	$K_3V_5O_{14}$,[45] $CaTa_4O_{11}$[46]
23	$[(3.4.5.4)^2, (3.5.4.5)^2]$	33.3/33.3/33.3	$Ba_3Si_4Ta_6O_{26}$ and $Ba_3Si_4Ta_6O_{23}$[47]
24	$[3.5.3.5, (3.4.5^2)^2]$	50/25/25	Ta_2O_5[48]
25	$[3.4.5.4, (3.4.5^2)^2]$	33.3/33.3/33.3	UVO_5[49]

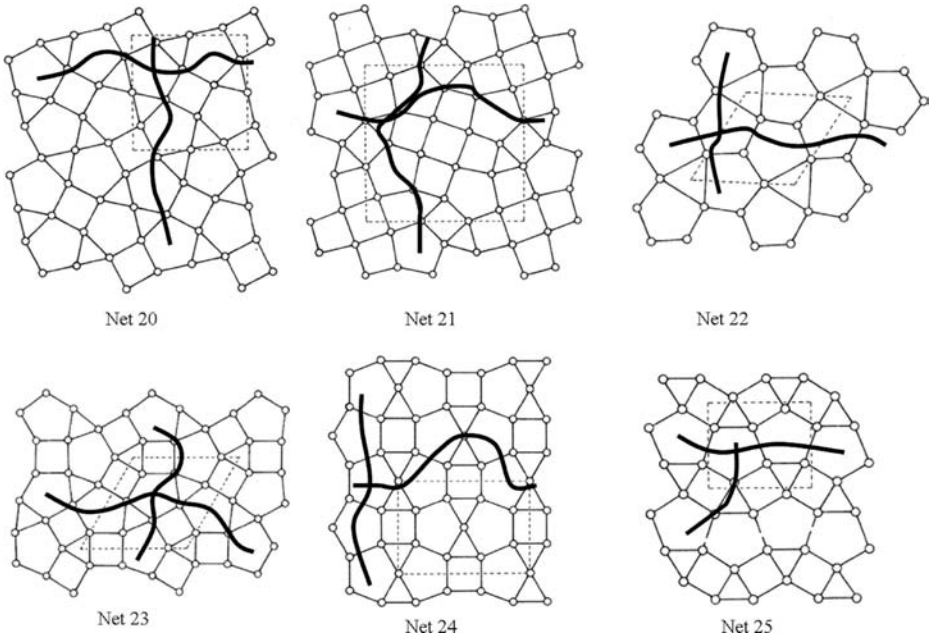

Figure 18. Ideal triangle−quadrangle−pentagon nets with lines showing likely preferred ion diffusion paths.

insight into the location of interstitial oxygen. A greater concentration of Nd than Ca (i.e., Nd/Ca > 1) leads to the introduction of mobile oxygen interstitials that fill the pentagonal rings of the tetrahedral layer. The $Ga^{I}O_4$ tetrahedron is connected via all four oxygen ions to tetrahedral dimers, while the $Ga^{II}O_4$ tetrahedron contains the nonbridging oxygen O^1 that provides the flexibility to accommodate interstitials through the repositioning of O^1 to enter the coordination environment of Ga^{II}, resulting in a distorted trigonal bipyramidal $Ga^{II}O_5$ polyhedron (Figure 15).[5] Stabilization of interstitial oxygen requires dynamical deformation of the framework that is an important feature of the modulated structure. Large cations at the A site can readily accommodate the change of coordination number,

and the corner-connected gallium oxide tetrahedral network can stabilize the interstitial oxygen by binding it into the polyhedral network. The preferred interstitial migration path along O^2 and O^3 is shown as oxygen ellipsoid elongation and excess electron density (Figure 16). Members of the flexible layered-structure melilite family can readily accommodate mobile interstitial oxygen.

CONCLUSION

Melilites contain a two-dimensional tetrahedral network with pentagons that are distorted even in the nonmodulated structures (e.g., $[SrNd]_2[Ga]_2[Ga_2O_7]_2$), but most evidently in the incommensurate form of $[CaNd]_2[Ga]_2[Ga_2O_7]_2$ (Figure 17). This long-range distortion enables the flexible deformation which is prerequisite for high interstitial oxygen mobility. Network systematics may be a powerful tool to predict modulation and also identify compounds as potential low-temperature ion conductors. Similar structures containing triangle−quadrangle−pentagon nets include (1) the $[(3.5.4.5)^2, 3.5.3.5]$ net as found for $Ca_5Al_6O_{18}$[41] and fresnoite types (such as $Ba_2TiSi_2O_8$,[42] $K_2MoAs_2O_9$,[43] and $K_2V_3O_8$[44]) that contain pentagons formed from alternate connections of tetrahedral dimers with pyramids TiO_5 (or Mo/VO_5), (2) the $[5.4^3, 5.4.3.4, 5.4^3, (5.4.3.4)^2]$ net as in $K_3W_5O_{15}$,[14] where five corner-connected tetrahedra form pentagon−triangle structures, with other tetrahedra edge-shared to form the extended network, (3) the $[(5^3.3)^2, 5^3, 5^3.3, 5^3]$ net for hexagonal structures such as $K_3V_5O_{14}$[45] and $CaTa_4O_{11}$,[46] (4) the $[(3.4.5.4)^2, (3.5.4.5)^2]$ net, such as $Ba_3Si_4Ta_6O_{26}$ and $Ba_3Si_4Ta_6O_{23}$,[47] where all tetrahedra are corner-connected, (5) the $[3.5.3.5, (3.4.5^2)^2]$ net, e.g., Ta_2O_5,[48] and (6) the $[3.5.3.5, (3.4.5^2)^2]$ net, as in UVO_5[49] (see Table 6). The connected pentagons are likely to provide favorable diffusion pathways for oxygen (Figure 18).[14] Other tetrahedral network candidates include one-dimensional nets such as Na_2SiO_3[50] and La_2TiO_5,[51] two-dimensional nets including $LaSrGaO_5$,[52] $Ba_2CuSi_2O_7$,[53] $Na_2Si_2O_5$,[54] $BaSi_2O_5$,[55] and nordite $LaSrNa_3ZnSi_6O_{17}$,[56] and three-dimensional nets as found in langasite $La_3Ga_5SiO_{14}$,[57] where a two-dimenional tetrahedral net is connected through octahedra.

In the present case, nonbridging oxygen O^1 in $Ga^{II}O_4$ serves as a key for the interstitial stabilization and mobility in melilite, and in general, modulated structures with terminal oxygen and a distorted network are potential candidates for high oxide mobility. Many well-known oxide ion conductors such as fresnoite[58] and fergusonite (e.g., $CeNbO_{4+x}$)[12] are all layered structures. $Ba_{18}Al_{12}O_{36}$[41] also has tetrahedra containing terminal oxygen. One other possible electrolyte is the bismuth calcium aluminate $Bi_2Ca_6Al_{12}O_{27}$,[59] where corner-connected AlO_4 tetrahedra form corrugated six- and three-membered rings, edge-sharing with CaO_8 polyhedra aligned along c that create three-dimensional nets, with Bi located in large hexagonal tunnels parallel to c to form Bi_2O_3 pairs. Another target ceramic may be $Na_2Si_3O_7$,[60] which is a (3 + 1) dimensional incommensurate structure with distorted silicate tetrahedral layers connected by Na. Certain brownmillerites (e.g., $Ca_2Fe_2O_5$)[61] are also incommensurate structures with distorted tetrahedral chains that are ready to accommodate interstitials. Moreover, further reduction of brownmillerites can form infinite-layer oxides ($Sr/CaFeO_2$) with square-planar oxygen coordination that have very high oxygen mobility.[62,63] Material families sharing these key crystal chemical features with melilite are potential fast oxide ion conductors.

ASSOCIATED CONTENT

Supporting Information. CIF data for average and modulated structure $[CaNd]_2[Ga]_2[Ga_2O_7]_2$. This material is available free of charge via the Internet at http://pubs.acs.org.

AUTHOR INFORMATION

Corresponding Author
tbaikie@ntu.edu.sg

ACKNOWLEDGMENT

We express our sincere gratitude to Professor Sander van Smaalen, University of Bayreuth, Germany, and Dr. V. Patříček, Institute of Physics Academy of Science, Czech Republic, for checking the JANA2006 refinement. This research work is funded by the Singapore MOE Tier2 Grant "Incommensuration in Oxide Crystal Structures: Impacts on Photocatalysis and Ion Conduction" (M4507008).

REFERENCES

(1) Minh, N. Q. *J. Am. Ceram. Soc.* **1993**, *76* (3), 563–588.
(2) Goodenough, J. B. *Nature* **1999**, *404*, 821–822.
(3) León-Reina, L.; Losilla, E. R.; Martinez-Lara, M.; Bruque, S.; Aranda, M. A. G. *J. Mater. Chem.* **2004**, *14*, 1142–1149.
(4) Packer, R. J.; Tsipis, E. V.; Munnings, C. N.; Kharton, V. V.; Skinner, S. J.; Frade, J. R. *Solid State Ionics* **2006**, *177*, 2059–2064.
(5) Kuang, X. J.; Green, M. A.; Niu, H. H.; Zajdel, P.; Dickinson, C.; Claridge, J. B.; Jantsky, L.; Rosseinsky, M. J. *Nat. Mater.* **2008**, *7*, 498–504.
(6) Raj, E. S.; Skinner, S. J.; Kilner, J. A. *Solid State Ionics* **2005**, *176*, 1097–1101.
(7) van Smaalen, S. *Incommensurate Crystallography*; Oxford University Press: New York, 2007.
(8) de Pater, C. J.; Helmholdt, R. B. *Phys. Rev. B* **1979**, *19* (11), 10.
(9) Boudard, M.; de Boissiu, M.; Janot, C.; Heger, G.; Beeli, C.; Nissen, H. U.; Vincent, H.; Ibberson, R.; Audier, M.; Duboiis, J. M. *J. Phys.: Condens. Matter* **1992**, *4*, 5.
(10) Petricek, V.; Gao, Y.; Lee, P.; Coppens, P. *Phys. Rev. B* **1990**, 42.
(11) Alberius-Henning, P. A.; Moustiakimov, M.; Lidin, S. *J. Solid State Chem.* **2000**, *150*, 154–158.
(12) Thompson, J. G.; Withers, R. L.; Brink, F. J. *J. Solid State Chem.* **1999**, *143*, 122–131.
(13) Rothlisberger, F.; Seifert, F.; Czank, M. *Eur. J. Mineral.* **1990**, *2*, 585–594.
(14) O'Keeffe, M.; Hyde, B. G. *Math. Phys. Sci.* **1980**, *295*, 553–623.
(15) Li, M. R.; Kuang, X. J.; Chong, S. Y.; Xu, Z. L.; Thomas, C. I.; Niu, H. J.; Claridge, J. B.; M.J., R. *Angew. Chem., Int. Ed.* **2010**, *49*, 2362–2366.
(16) Merwin, L. H.; Sebald, A.; Seifert, F. *Phys. Chem. Miner.* **1989**, *16*, 752–756.
(17) Hagiya, K.; Ohmasa, M. *Acta Crystallogr., B* **1993**, *49*, 172–179.
(18) Tamura, T.; Yoshiasa, A.; Iishi, K.; Takeno, S.; Maeda, H.; Emura, S.; Koto, K. *Phys. Chem. Miner.* **1996**, *23*, 81–88.
(19) Yang, H.; Hazen, R. M.; Downs, R. T.; Finger, L. W. *Phys. Chem. Miner.* **1997**, *24*, 510–519.
(20) Jiang, J. C.; Schosnig, M.; Schaper, A. K.; Ganster, K. *Phys. Chem. Miner.* **1998**, *26*, 128–134.
(21) Bagautdinov, B.; Hagiya, K.; Kusaka, K.; Ohmasa, M.; Iishi, K. *Acta Crystallogr., B* **2000**, *56*, 811–821.
(22) Bindi, L.; Bonazzi, P.; Dusek, M.; Petricek, V.; Chapuis, G. *Acta Crystallogr., B* **2001**, *57*, 739–746.
(23) Tealdi, C.; Mustarelli, P.; Islam, M. S. *Adv. Funct. Mater.* **2010**, *20*, 3874–3880.
(24) Thomas, C. I.; Kuang, X. J.; Deng, Z. Q.; Niu, H. J.; Claridge, J. B.; Rosseinsky, M. J. *Chem. Mater.* **2010**, *22*, 2510–2516.

(25) van Smaalen, S. *Z. Kristallogr.* **2004**, *219*, 681–691.
(26) Bruker. *TOPAS*, version 4.1; Bruker AXS Inc.: Madison, WI, 2008.
(27) Cheary, R. W.; Coelho, A. *J. Appl. Crystallogr.* **1992**, *25*, 109–121.
(28) Cheary, R. W.; Coelho, A. *J. Appl. Crystallogr.* **1998**, *31*, 851–861.
(29) Skakle, J. M. S.; Herd, R. *Powder Diffr.* **1999**, *14*, 195–202.
(30) Petricek, V.; Dusek, M.; Palatinus, L. *Jana2006. The Crystallographic Computing System*; Institute of Physics: Praha, Czech Republic, 2006.
(31) Sears, V. F. *International Tables for Crystallography*; Kluwer Academic Publishers: Dordrecht, The Netherlands, 1993.
(32) Janner, A.; Janssen, T.; de Wolff, P. M. *Acta Crystallogr., A* **1983**, *39*, 658–666.
(33) Bindi, L. *Rend. Lincei* **2008**, *19*, 1–15.
(34) Stokes, H. T.; Campbell, B. J.; van Smaalen, S. *Acta Crystallogr., A* **2011**, *67*, 45–55.
(35) Shannon, R. D. *Acta Crystallogr., A* **1976**, 32.
(36) Altermatt, D.; Brown, I. D. *Acta Crystallogr., B* **1985**, *41*, 244–247.
(37) Seifert, F.; Czank, M.; Simons, B.; Schmahl, W. *Phys. Chem. Miner.* **1987**, *14*, 26–35.
(38) Jia, Z. H.; Schaper, A. K.; Treutmann, W.; Rager, H.; Massa, W. *J. Cryst. Growth* **2004**, *273*, 303–310.
(39) Seifert, F.; Rothlisberger, F. *Mineral. Petrol.* **1993**, *48*, 179–192.
(40) Wong, C. L.; Ferraris, C.; White, T. J. *J. Solid State Chem.* **2011**, *184*, 1768–1776.
(41) Santamaria-Perez, D.; Vegas, A. *Acta Crystallogr., B* **2003**, *59*, 305–323.
(42) Moore, P. B.; Louisnathan, J. *Science* **1967**, *156*, 1361–1362.
(43) Zid, M. F.; Jouini, T. *Acta Crystallogr., C* **1996**, *52*, 1334–1336.
(44) Chakoumakos, B. C.; Cutselcean, R.; Kamiyama, T.; Oikawa, K.; Sales, B. C.; Lumsden, M. D. *J. Solid State Chem.* **2007**, *180*, 812–817.
(45) Byström, A. M.; Evans, H. T. J. *Acta Chem. Scand.* **1959**, *13*, 377–378.
(46) Johnberg, L. *J. Solid State Chem.* **1970**, *1*, 454–462.
(47) Shannon, J.; Katz, L. *J. Solid State Chem.* **1970**, *1*, 399–408.
(48) Stephenson, N. C.; Roth, R. S. *Acta Crystallogr., B* **1971**, *27*, 1037–1044.
(49) Marnider, B. *Acta Chem. Scand.* **1990**, *44*, 123–134.
(50) Liu, F.; Garofalini, S. H.; King-Smith, R. D.; Vanderbilt, D. *Chem. Phys. Lett.* **1993**, *215*, 401–404.
(51) Martín-Sedeño, M. C.; Marrero-López, D.; Losilla, E. R.; León-Reina, L.; Bruque, S.; Núñez, P.; Aranda, M. A. G. *Chem. Mater.* 2005, *17*, 5989–5998.
(52) Gesing, T. M.; Uecker, R.; Buhl, J. C. *Eitschrift Kristallogr.—New Cryst. Struct.* **2000**, *215*, 413–418.
(53) Armbruster, T. *Am. Mineral.* **1990**, *75*, 847–858.
(54) Fleet, M. E.; Henderson, G. S. *J. Solid State Chem.* **1995**, *119*, 400–404.
(55) Goreaud, M.; Choisnet, J.; Raveau, B.; Deschanvres, A. *Rev. Chim. Miner.* **1974**, *11*, 207–216.
(56) Bakakin, V. V.; Belov, N. V.; Borisov, S. V.; Solovyeva, L. P. *Am. Mineral.* **1970**, *55*, 1167.
(57) Belokoneva, E. L.; Stefanovich, S. Y.; Pisarevskii, Y. V.; Mosunov, A. V. *Russ. J. Inorg. Chem.* **2000**, *45*, 1642–1651.
(58) Bindi, L.; Dusek, M.; Petricek, V.; Bonazzi, P. *Acta Crystallogr., B* **2006**, *62*, 1031–1037.
(59) Pérez, O.; Malo, S.; Hervieu, M. *Acta Crystallogr., B* **2010**, *66*, 585–593.
(60) Krüger, H.; Kahlenberg, V.; Friese, K. *Acta Crystallogr., B* **2006**, *62*, 547–555.
(61) Krüger, H.; Kahlenberg, V. *Acta Crystallogr., B* **2005**, *61*, 656–662.
(62) Hayward, M. A.; Rosseinsky, M. J. *Nature* **2007**, *450*, 960–961.
(63) Inoue, S.; Kawai, M.; Ichikawa, N.; Kageyama, H.; Paulus, W.; Shimakawa, Y. *Nat. Chem.* **2007**, *2*, 213–217.